Widespread excess ice in Arcadia Planitia, Mars

Ali M. Bramson[1], Shane Byrne[1], Nathaniel E. Putzig[2], Sarah Sutton[1], Jeffrey J. Plaut[3], T. Charles Brothers[4], and John W. Holt[4]

[1]Lunar and Planetary Laboratory, University of Arizona, Tucson, Arizona, USA, [2]Southwest Research Institute, Boulder, Colorado, USA, [3]Jet Propulsion Laboratory, Pasadena, California, USA, [4]Institute for Geophysics, University of Texas at Austin, Austin, Texas, USA

Abstract The distribution of subsurface water ice on Mars is a key constraint on past climate, while the volumetric concentration of buried ice (pore-filling versus excess) provides information about the process that led to its deposition. We investigate the subsurface of Arcadia Planitia by measuring the depth of terraces in simple impact craters and mapping a widespread subsurface reflection in radar sounding data. Assuming that the contrast in material strengths responsible for the terracing is the same dielectric interface that causes the radar reflection, we can combine these data to estimate the dielectric constant of the overlying material. We compare these results to a three-component dielectric mixing model to constrain composition. Our results indicate a widespread, decameters-thick layer that is excess water ice $\sim 10^4 \, km^3$ in volume. The accumulation and long-term preservation of this ice is a challenge for current Martian climate models.

1. Introduction

Information on past Martian climates is contained within the distribution and volume fraction of water ice. The conventional picture of Amazonian midlatitude ice is that it is young and pore-filling ground ice, which responds quickly to varying orbital and climatic conditions via atmospheric exchange [*Mellon and Jakosky*, 1993; *Schorghofer and Aharonson*, 2005; *Hudson et al.*, 2007; *Bryson et al.*, 2008]. Throughout the last 3 Gyr of Mars' history, these orbital variations dictate where ice is stable—with ice locked up at the poles during low obliquities and mobilized to lower latitudes during higher obliquities [*Head et al.*, 2003].

Models of the distribution of ice stability with the current Martian climate (and today's lower-than-average obliquity) suggest that water ice should be stable poleward of the midlatitudes (~40–50°) within a meter of the surface and stable closer to the surface near the poles [*Mellon et al.*, 2004; *Schorghofer*, 2007]. These predictions are supported by inferences of water-equivalent hydrogen content in the upper meter of the surface using the Gamma Ray Spectrometer and Neutron Spectrometer on board Mars Odyssey [*Boynton et al.*, 2002; *Feldman et al.*, 2002; *Mitrofanov et al.*, 2002].

The current consensus is that ice in the northern midlatitudes should be "pore filling," accumulating in and sublimating from shallow pore spaces in the regolith in equilibrium with atmospheric water vapor. However, multiple observations suggest relatively pure excess ice, with higher ice abundances than possible within the porosity of dry regolith. Evidence includes ice-exposing impacts [*Byrne et al.*, 2009; *Dundas et al.*, 2014], radar detection of massive ice in debris-covered glaciers [*Holt et al.*, 2008; *Plaut et al.*, 2009a], analysis of the latitude dependence of pedestal craters [*Kadish et al.*, 2009], and thermokarstic expansion of secondary craters [*Viola et al.*, 2015]. The Phoenix lander (at 69°N) excavated both pore filling and excess ice in the upper centimeters of the surface [*Mellon et al.*, 2009; *Smith et al.*, 2009].

Neither the source nor the emplacement timing of excess ice in the midlatitudes is well understood. A recent study by *Viola et al.* [2015] of superposed secondary craters in Arcadia Planitia suggests excess ice in this location that is tens of millions of years old. This age is inconsistent with ice stability models, which predict that any ice should periodically sublimate away with obliquity cycles that vary on much shorter time scales. Proposed formation mechanisms for excess ice include burial and preservation of snowpack or glaciers from past orbital periods [*Head et al.*, 2003; *Levrard et al.*, 2004; *Schorghofer*, 2007; *Holt et al.*, 2008; *Schorghofer and Forget*, 2012], development of ice lenses in the subsurface [*Sizemore et al.*, 2015], and thermal contraction of ice in pore spaces to allow increased water vapor diffusion [*Fisher*, 2005].

Understanding ice-emplacement mechanisms and timing is important for understanding Martian climate history. However, to do so one must first constrain the current distribution and concentration of subsurface
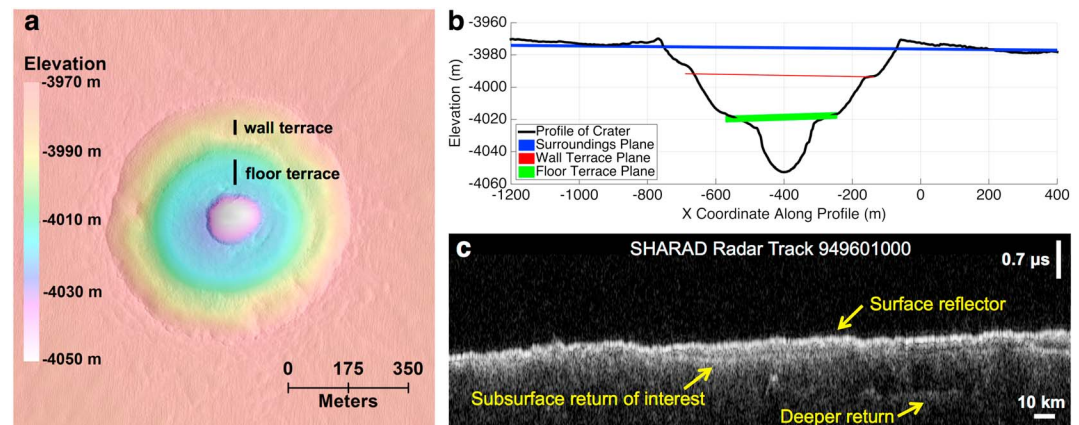
Figure 1. (a) DTM for a doubly terraced crater (informally known as Badger Crater) made with HiRISE images ESP_018522_2270 and ESP_019010_2270. (b) Profile across the crater with planes fit to elevations sampled across the surroundings and each terrace. (c) SHARAD radargram that passes within 8.2 km of Badger crater with vertical scale given in one-way travel time.

ice on Mars. Craters provide a way to probe subsurface structure, and concentric terracing within the walls of simple craters (Figure 1) is often indicative of layering within the target material [*Quaide and Oberbeck*, 1968; *Ormö et al.*, 2013]. Here we use images and digital terrain models (DTMs) from the Mars Reconnaissance Orbiter (MRO) High Resolution Imaging Science Experiment (HiRISE) [*McEwen et al.*, 2010] to determine the morphology and geometry of terraced craters within Arcadia Planitia, and we combine these data with radar sounding from the MRO Shallow Radar (SHARAD) instrument (Figure 1c) to constrain the dielectric properties (and thus composition) of the materials overlying a widespread, radar-detected interface.

2. Methods

We mapped the locations of 187 terraced craters within Arcadia Planitia (Figure 2) using 281 Context Camera (CTX) [*Malin et al.*, 2007] images within the region between 180°E–225°E and 38°N–50°N, chosen on the basis of the boundary within which *Plaut et al.* [2009b] initially found a widespread SHARAD reflector indicative of layering within the subsurface. We projected CTX images using the United States Geological Survey's ISIS (Integrated Software for Imagers and Spectrometers) and Map Projection on the Web tools and imported the projected images at full resolution into Esri's geospatial processing program ArcMap™.

We termed a crater as terraced if it exhibited a concentric, flat-lying ledge within the crater wall. Craters were given one of three designations based on the number of terraces and the certainty of terracing: one terrace, two terraces, or questionable terracing. We assigned the latter designation if, at CTX resolution (6 m/pixel), the possible terraces were not pronounced, the concentric structure was only seen in part of the crater, or if the morphology was difficult to distinguish from an expanded crater morphology (as defined by *Viola et al.* [2015]). We followed up on 32 of these terraced craters with HiRISE stereo imaging. From these stereo data, we made 11 DTMs (Figure S3 in the supporting information) using a combination of ISIS and the stereogram-metric SOCET SET™ (BAE Systems, Inc.) software, following the method described in *Kirk et al.* [2008] and *Sutton et al.* [2015]. From the DTMs, we sampled the elevations of each terrace at multiple azimuths as well as the surrounding terrain at three crater radii from the crater's center (beyond most ejecta). We fit planes to these elevations for both surroundings and terrace(s), calculating the elevation on each plane at the center of the crater. We recorded the depth of a terrace as the difference between the elevation of the surrounding and terrace planes at the crater's center (details of all measurements are in Table S1 in the supporting information).

We also mapped the surface and subsurface radar interfaces across Arcadia Planitia in 299 SHARAD tracks. These radargrams (along-track images of radar return power versus delay time) were processed with the Smithsonian focused processor [*Campbell et al.*, 2011] on the Colorado SHARAD Processing System (CO-SHARPS) using the processing parameters listed in Text S1 in the supporting information. With its 20 MHz center frequency and bandwidth of 10 MHz, SHARAD provides a vertical resolution of 15 m in free space and $15\,\varepsilon_r^{-1/2}$ m in a medium of a given dielectric constant (ε_r).
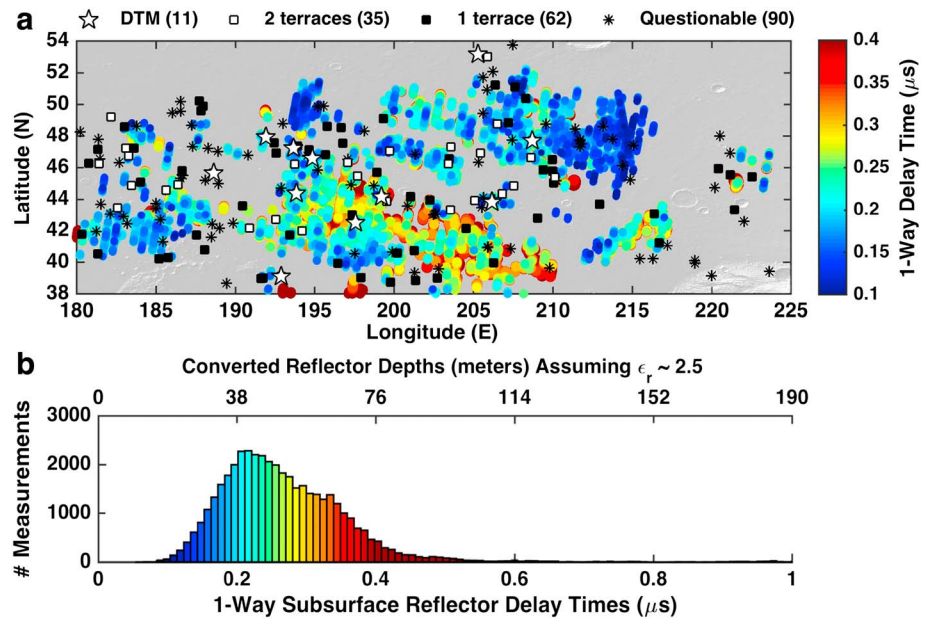
Figure 2. (a) Terraced crater locations (B&W) and SHARAD one-way delay times (colors) of mapped subsurface interfaces. (b) One-way delay times in Figure 2a.

Bright reflections from off-nadir surface topography, known as "clutter," may appear at the same delay times as subsurface returns in the radar data. To check for clutter, we compared the radargrams to corresponding clutter simulations produced using the algorithm of *Holt et al.* [2006, 2008] with Mars Orbiter Laser Altimeter (MOLA) data (Figure S1). We mapped nonclutter subsurface reflectors using SeisWare geophysical interpretation software (SeisWare International Inc.), avoiding radar sidelobes using methods described in Text S1.

Assuming that the change in material strength responsible for the terraces corresponds to the dielectric interface that causes the subsurface SHARAD reflection, we can use the terraced crater geometry to independently measure the depth to the subsurface reflector. For each crater, we calculated an inverse-distance weighted mean for all one-way delay times (half of the measured delay times) between the surface and subsurface reflectors within 10 km of the crater. Comparing the depth of the terraces (Δx) to the time delay between surface and subsurface radar reflections (Δt), we determined wave velocity (v) and thus the dielectric constant (relative dielectric permittivity) of the overlying material near the craters: $\varepsilon_r = (c\,\Delta t/\Delta x)^2 = (c/v)^2$, where c is the speed of light in vacuum. Text S2 contains our method of estimating errors in ε_r.

The dielectric constant is a measure of how effectively an electromagnetic wave can move in a material relative to free space and varies with material properties. Thus, our calculations put constraints on the composition of the radar-transmitting layer. The dielectric constant of pure water ice is ~3.15 [*Matsuoka et al.*, 1997] while that of vacuum (and the Martian atmosphere) is 1. *Rust et al.* [1999] found an ε_r of 7.54 for pure basalt (no porosity included), while *Campbell and Ulrichs* [1969] found values up to ~9 for bulk measurements of dense basalts; for this work, we follow *Moore and Jakosky* [1989] in assuming an ε_r of 8 for any lithic material. We compare our ε_r estimates near the terraced craters to the modeled dielectric behavior for three-component mixtures of varying volumetric fractions of ice, basaltic rock, and air (i.e., empty pore space) using the power law relation $\varepsilon_{mix}^{1/\gamma} = v_{rock}\varepsilon_{rock}^{1/\gamma} + v_{ice}\varepsilon_{ice}^{1/\gamma} + v_{air}\varepsilon_{air}^{1/\gamma}$ with $\gamma = 2.7$, the exponent *Stillman et al.* [2010] found to best fit sand-ice mixtures (Figure 3). *Shabtaie and Bentley* [1994] showed that $\gamma = 2.7$ also works for ice-air mixtures, and this fit should hold for inclusions of any dielectrically inert material (which covers the range of expected Martian materials) [*Stillman and Olhoeft*, 2008].

The compositions predicted by the dielectric mixing models yield nonunique solutions. For example, pure water ice has a dielectric constant of ~3.15; however, Figure 3 demonstrates that this value would also be consistent with a mixture of about equal parts rock and air or a three-component mixture of about 50% ice, 25% rock, and 25% air (as well as a variety of mixtures in between).
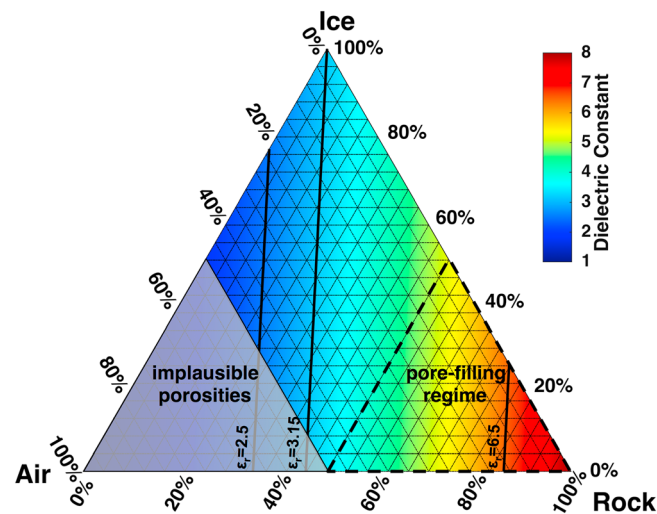
Figure 3. Ternary diagram of dielectric constant calculations for mixtures of ice, rock, and air. The shaded bottom left corner represents the region of parameter space where porosities are implausible (>50%). The bottom right corner inside the dashed lines is the pore-filling ice regime. The near-vertical bold lines represent the contours for three dielectric constant values (2.5, 3.15, and 6.5).

Porosities of more than 50% (bottom left of Figure 3) are rare in geologic materials. Porosity is expected to be at a maximum at the surface, and modeling by *Zent et al.* [2010] for the Phoenix landing site and measurements taken at the Viking landing sites of loose winddrift material [*Moore et al.*, 1987] suggest a surface porosity of ~50%. Windblown material is likely not representative of actual regolith though. Recent gravity measurements of porosity in the near-surface lunar regolith are significantly lower, ~10–20% [*Wieczorek et al.*, 2013; *Han et al.*, 2014]. Therefore, we adopt the Viking surface measurement as a conservative upper limit for the porosities averaged over decameters into the subsurface.

The bottom right corner of Figure 3 represents the regime of porous regolith with varying amounts of ice filled into the pore spaces. The lines along values of constant rock content represent a continuum ranging from empty pore spaces at the bottom of the plot (the line defining 0% ice) to completely ice-filled pores (where the rock-content line intersects with 0% air).

3. Results

Many of the craters included in this study exhibit two terraces, with a shallower, subtler terrace within the crater wall and a wider, deeper terrace near the floor of the crater. As the shallower terraces are less pronounced, we interpret this as a subtler change in material properties—which is less likely to be detected with SHARAD. Within the area searched with CTX images, we identified 62 craters (diameter = 328 ± 129 m within one standard deviation) as single terraced and 35 craters (diameter = 430 ± 135 m) as having two terraces. We categorized an additional 90 craters (diameter = 339 ± 271 m) as "questionably terraced."

Figure 1a shows a DTM for one such doubly terraced crater (informally named Badger) located at 46.581°N, 194.85°E. Its large, flat terrace is at 43 m depth (which we term floor level) and likely a major compositional interface. A smaller, shallower (17 m depth) terrace in the crater wall suggests additional complexity in the subsurface, perhaps a change in porosity or composition (such as a desiccated surface layer overlying ice). The fact that we see many craters with two terraces (which on average probe deeper than single-terraced craters) suggests that there are multiple layers within the subsurface throughout this region. The similarity in terracing across many craters indicates that the same subsurface structure likely extends across the study area. However, the spread in terrace depths (Table S1) indicates significant heterogeneity in the thicknesses of the material. Our terrace depths generally cluster into three or four depth ranges (<10 m, 17–23 m, 26–31 m, and >42 m).

Our results from mapping SHARAD reflectors also show lateral heterogeneity, with greater delay times toward the south and interspersed patches that lack subsurface reflectors. We do not see any cases with two subsurface SHARAD interfaces that may be associated with the terraces, although there is occasionally a much deeper reflector beyond the depths probed by the craters (an example of which can be seen in Figure 1c). This deeper reflector is interpreted as the continuation of a buried Vastitas Borealis Formation unit often seen across Amazonis Planitia [*Campbell et al.*, 2008], which is directly south of our region of interest in Arcadia Planitia. Since this deeper reflector is related to a separate geological contact, we purposefully avoided mapping it in Arcadia Planitia, although it is possible that in rare places this reflector could have been the only one present and therefore misinterpreted. Figure 2b shows a histogram of measured one-way delay

times for the entire study area, with the peak at 0.22 μs. The tail of large delay times may be contamination from this buried Vastitas Borealis Formation contact.

The extent of our mapped SHARAD reflectors is similar to that initially found by *Plaut et al.* [2009b] and *Stillman and Grimm* [2011]. We compute the area of Arcadia Planitia that contains a mapped subsurface radar reflector to be ~2.5×10^5 km². Our map of subsurface reflectors (Figure 2a) shows a small gap near 212°E, 40°N, where the surface echo is absent due to unusually high roughness (also indicted in MOLA pulse width data) [*Carter et al.*, 2009b], preventing an accurate measure of delay time to the subsurface reflector. Similar behavior is seen by SHARAD in the Medusae Fossae Formation where the surface is extremely rough between centimeter and meter scales and the low dielectric constant limits the power of the surface return [*Carter et al.*, 2009b]. Because of this and additional reasons discussed below, the extent of the deposit shown in Figure 2a is a lower limit. We also compute a convex hull of 1.2×10^6 km² around the subsurface radar reflector measurements to put an upper limit on the area enclosed by the detections (details in Text S3).

We believe that the real geographic area covered by the deposit is closer to that calculated for the convex hull (upper bound) than for the mapped radar reflector (lower bound) because the deposit likely occurs even in reflection-free patches. We are not able to resolve any interfaces from within the vertical resolution of SHARAD (8.4 m assuming pure water ice of $\varepsilon_r = 3.15$ or 5.3 m in rock with $\varepsilon_r = 8$). Efforts to limit sidelobes of the surface echo can also preclude the identification of any other shallow reflectors within ~20–30 m of the surface, potentially obscuring the multiple shallower reflectors that one might otherwise expect to occur given the terracing seen within the crater walls. The deepest terraces within two craters located in areas where no SHARAD subsurface reflection appears are at 18 and 23 m depths, likely within this near-surface range where subsurface returns may be masked by the bright surface return or attenuated in the processing to limit sidelobes. Because we find terraced craters in some of these subsurface-reflector-free patches, it is probable that the layer does not disappear when the reflector disappears but rather the interface becomes too shallow for its base to be resolved by the radar. Reflection-free patches could also be produced by a small dielectric contrast between overlying and underlying materials or a gradual vertical dielectric transition.

Two SHARAD tracks pass near the crater shown in Figure 1 with one-way delay times of the subsurface reflector ranging from 0.21 μs to 0.27 μs. Using an inverse-distance weighted mean of radar returns within 10 km gives a one-way delay time of 0.24 μs relative to the surrounding surface. If the SHARAD interface corresponds to the small, shallower terrace at 17 m depth, then $\varepsilon_r = 17.9 \pm 0.39$, an unrealistically large value for geologic materials. Thus, it is implausible that the radar reflector corresponds to this upper compositional interface. However, associating this delay time with the second, deeper terrace at a depth of 43 m yields a realistic $\varepsilon_r \sim 2.9 \pm 0.39$. This is consistent with our expectation that the deeper, more significant, terraces are more likely to correspond to the radar reflection. Therefore, we compare the deeper terraces to subsurface radar returns. Four out of the 11 terraced craters for which we have DTMs exhibit two terraces (important because we require the deeper terrace) and have subsurface radar reflectors within 10 km (important because of the lateral heterogeneity in the thickness of the layer). For three of these craters, we find similar dielectric constants of 2.1, 2.6, and 2.9.

The fourth crater yields a higher dielectric constant of 6.5 (rightmost contour in Figure 3), but this crater is likely too shallow to provide realistic interpretations of the layer. An ε_r of 6.5 is a reasonable value for pore-filling ice or porous basalt, a common material on Mars that is often layered. However, this crater's deepest terrace is at 31 m, whereas the other three have floor terraces deeper than 42 m. Thus, this fourth crater likely does not excavate to sufficient depth to intersect the radar reflector interface despite it having two terraces, and the measurements from the other three craters are expected to be most representative of the bulk composition of the layer.

The average dielectric constant of the three deepest craters is 2.5 with an error of 0.28. Because our $\varepsilon_r = 2.5$ contour is clearly outside the pore-filling ice parameter space (Figure 3), we conclude that the material in the upper decameters of the surface is excess ice of up to 75% volumetric fraction ice. Because we can only compute a bulk dielectric constant from surface to base of the radar-detected subsurface interface, this value likely includes the effects of a desiccated regolith layer at the surface, which could bias the interpretation toward lower ice contents. Our results can only place constraints on the overall composition, ignoring the finer structure that likely exists in the upper decameters of the subsurface. Using this average dielectric

constant, we convert delay times to depths to constrain the volume of the deposit to be between $\sim 1.3 \times 10^4$ km^3 and 6.1×10^4 km^3 (see Text S3 for details).

For the $\varepsilon_r = 2.5$ contour, the maximum allowed volumetric rock fraction is ~20%, meaning the initial porosity would have to be 80% if the ice were deposited via the usual pore-filling ice mechanism. Even at the high-end of our error bars, where the maximum rock fraction reaches 30%, the initial porosity would need to be ~70%. These are unreasonable initial porosities, and thus, we rule out the atmospheric vapor pore-filling ice origin.

Dielectric constants as low as ~3.0 can be due to low-density volcanic materials such as pumice, tuff, and ash [*Campbell and Ulrichs*, 1969]. Such dielectric constants have been measured in the upper few hundred meters of the Medusae Fossae Formation and were interpreted to be a low-density pyroclastic unit [*Watters et al.*, 2007; *Carter et al.*, 2009b]. While similarly porous volcanic materials could explain the dielectric constants in Arcadia Planitia, one cannot explain other morphological features such as expanded craters [*Viola et al.*, 2015] or the ice-exposing craters [*Dundas et al.*, 2014] with such materials.

Carbon dioxide ice has a dielectric constant of ~2.1 [*Pettinelli et al.*, 2003]. While our calculations yield numbers that could also be consistent with CO_2 ice and lithic mixtures, the temperature decameters into the subsurface will equal the annual mean surface temperature, which is much greater than the frost point for CO_2 ice. Thus, conditions at the midlatitudes are not stable for perennial buried CO_2 ice, and we rule out this composition.

The SHARAD subsurface reflectors we detect across Arcadia Planitia are of similar brightness to the surface reflector, suggesting that this subsurface layer does not strongly attenuate the signal, behaving similarly to reflectors in the polar layered deposits [*Putzig et al.*, 2009] and the base of lobate debris aprons [*Holt et al.*, 2008; *Plaut et al.*, 2009a]. This provides additional support in favor of an ice-rich layer rather than a lithic-rich layer, as lithic materials cause more attenuation of the radar return [*Carter et al.*, 2009a, 2009b]. Although there are numerous interpretations that would match our calculations, the prevalence of surface features associated with the presence of excess ice across Arcadia Planitia [*Holt et al.*, 2008; *Byrne et al.*, 2009; *Kadish et al.*, 2009; *Plaut et al.*, 2009a; *Dundas et al.*, 2014; *Viola et al.*, 2015] also supports our ice interpretation.

4. Conclusions and Discussion

We present evidence of widespread subsurface layering from SHARAD radar interfaces and terraced craters across Arcadia Planitia. We use HiRISE-derived digital terrain models of terraced craters to directly measure the depths to this SHARAD interface. From the combination of depths and radar delay times, we calculate dielectric constants and infer that the decameters of material between the surface and interface is mostly water ice. Our work constrains depths to the presumed base of the ice layer (mode depth = 42 m, mean depth = 51 m, standard deviation = 18 m, using our derived dielectric constant of 2.5). We also place constraints on the area covered by the ice ($<1.2 \times 10^6$ km^2) over a latitude range of 38°N–52°N and place limits on the volume of ice (1.3×10^4 km^3–6.1×10^4 km^3). Superposed expanded secondary craters in the region also support the presence of excess ice, and dating of their primary craters suggests that this ice has been present at this location for tens of millions of years [*Viola et al.*, 2015].

Climate models suggest that widespread deposition of ice could have occurred in the midlatitudes during Mars' high-obliquity (>35°) periods under certain conditions; e.g., *Madeleine et al.* [2009] found that ~10 mm/yr of ice accumulation was possible in Arcadia Planitia when equatorial "tropical mountain glacier" ice is available to be mobilized, atmospheric dust opacity is high ($\tau = 2.5$), and obliquity is 35°. Any such period of ice deposition/snowfall would likely need to be quickly followed by the formation of a protective lag to preserve the layer. However, uncertainty exists in conditions needed to preserve the layer for the tens of millions of years suggested by *Viola et al.* [2015].

The response of ice to changing conditions is dependent on the diffusion coefficient of water vapor through the regolith, with higher-diffusion coefficients corresponding to faster responses. Experimental studies of ice diffusion properties under simulated Martian conditions suggest that Martian regolith has high-diffusion coefficients [*Chevrier et al.*, 2007; *Hudson et al.*, 2007; *Bryson et al.*, 2008; *Sizemore and Mellon*, 2008]; in other words, water vapor should readily diffuse from the subsurface during even brief excursions through periods of ice instability. Evidence that ice in the upper meter of the surface responds rapidly to climatic changes comes from Mars Odyssey observations [*Boynton et al.*, 2002; *Feldman et al.*, 2002; *Mitrofanov et al.*, 2002],

which show a match between today's ice distribution and current climate model predictions [*Mellon et al.*, 2004; *Schorghofer and Aharonson*, 2005]. Depths to ice at the Phoenix site suggest that the extent of ground ice is in approximate equilibrium with the present climate [*Mellon et al.*, 2009].

With such findings, a mechanism to preserve an ice sheet for tens of millions of years remains elusive. Experiments by *Hudson et al.* [2007] have difficulty attaining the low-diffusion coefficients needed to preserve ice for this long. Laboratory experiments on mass loss rates of pure water ice by *Bryson et al.* [2008] find that a 1 m layer of ice underneath a 2 m layer of fine-grained basaltic regolith could remain stable for 400 kyr (since the last large obliquity change). It is unclear from their study, however, if thicker ice could remain through the hundreds of predicted large obliquity changes over the course of the last tens of millions of years. *Head et al.* [2003] and *Schorghofer and Forget* [2012] predict that a thick ice sheet would be geologically recent and actively retreating to come into equilibrium with the current atmospheric conditions at these midlatitudes. For example, ice stability models by *Schorghofer and Forget* [2012] found that a 4.5 Myr old ice sheet (an order of magnitude younger than this ice) 30 m thick and extending to the equator would not have survived at these latitudes to the present day.

While atmospheric water vapor can recharge the ice within pore spaces quickly, once excess ice has sublimated away, it cannot be recharged via atmospherically derived water. *Fisher* [2005] proposed a mechanism by which thermal contraction of pore ice works to open voids that can be further filled with ice through diffusion of water vapor. His results suggest that the upper few meters of Martian regolith could reach up to 70% ice by mass in 10 Myr. But it is doubtful that this mechanism could form the thicknesses of excess ice at the depths we infer to be present across Arcadia Planitia.

Segregation of preexisting pore ice, analogous to frost heave, has also been proposed for generating excess ice near the surface by *Sizemore et al.* [2015], who modeled ice lens initiation and development, tracking phase partitioning of water in soil pores. Their simulations suggest that ice lens formation is possible in the upper tens of centimeters of the surface in fine-grained soils. However, the thicknesses of ice discussed in this paper are likely too great to form from ice lenses, even under idealized soil and temperature conditions with continuous growth of segregated ice.

We consider snowfall to be the leading formation mechanism proposed for this ice deposit because it can most easily explain the thickness and widespread nature of the excess ice observed. An ice deposition episode similar to that proposed by *Madeleine et al.* [2009] would be a good candidate for the excess ice across Arcadia Planitia, but because of the expected age of the ice, there is a need for a theoretical paradigm to explain its preservation. The latitude range of this ice deposit, its purity, thickness, area, and volume provide important constraints for future climate and ice stability models over the last tens of millions of years.

References

Boynton, W. V., et al. (2002), Distribution of hydrogen in the near surface of Mars: Evidence for subsurface ice deposits, *Science*, *297*, 81–85, doi:10.1126/science.1073722.

Bryson, K. L., V. Chevrier, D. W. G. Sears, and R. Ulrich (2008), Stability of ice on Mars and the water vapor diurnal cycle: Experimental study of the sublimation of ice through a fine-grained basaltic regolith, *Icarus*, *196*, 446–458, doi:10.1016/j.icarus.2008.02.011.

Byrne, S., et al. (2009), Distribution of mid-latitude ground ice on Mars from new impact craters, *Science*, *325*, 1674–1976, doi:10.1126/science.1175307.

Campbell, B. A., N. E. Putzig, L. M. Carter, and R. J. Phillips (2011), Autofocus correction of phase distortion effects on SHARAD echoes, *IEEE Geosci. Remote Sens. Lett.*, *8*(5), 939–942, doi:10.1109/LGRS.2011.2143692.

Campbell, B., L. Carter, R. Phillips, J. Plaut, N. Putzig, A. Safaeinili, R. Seu, D. Biccari, A. Egan, and R. Orosei (2008), SHARAD radar sounding of the Vastitas Borealis Formation in Amazonis Planitia, *J. Geophys. Res.*, *113*, E12010, doi:10.1029/2008JE003177.

Campbell, M. J., and J. Ulrichs (1969), Electrical properties of rocks and their significance for lunar radar observations, *J. Geophys. Res.*, *74*(25), 5867–5881, doi:10.1029/JB074i025p05867.

Carter, L. M., B. A. Campbell, J. W. Holt, R. J. Phillips, N. E. Putzig, S. Mattei, R. Seu, C. H. Okubo, and A. F. Egan (2009a), Dielectric properties of lava flows west of Ascraeus Mons, Mars, *Geophys. Res. Lett.*, *36*, L23204, doi:10.1029/2009GL041234.

Carter, L. M., et al. (2009b), Shallow Radar (SHARAD) sounding observations of the Medusae Fossae Formation, Mars, *Icarus*, *199*, 295–302, doi:10.1016/j.icarus.2008.10.007.

Chevrier, V., D. W. G. Sears, J. D. Chittenden, L. A. Roe, R. Ulrich, K. Bryson, L. Billingsley, and J. Hanley (2007), Sublimation rate of ice under simulated Mars conditions and the effect of layers of mock regolith JSC Mars-1, *Geophys. Res. Lett.*, *34*, L02203, doi:10.1029/2006GL028401.

Dundas, C. M., S. Byrne, A. S. McEwen, M. T. Mellon, M. R. Kennedy, I. J. Daubar, and L. Saper (2014), HiRISE observations of new impact craters exposing Martian ground ice, *J. Geophys. Res. Planets*, *119*, 109–127, doi:10.1002/2013JE004482.

Feldman, W. C., et al. (2002), Global distribution of neutrons from Mars: Results from Mars Odyssey, *Science*, *297*, 75–78, doi:10.1126/science.1073541.

Fisher, D. (2005), A process to make massive ice in the Martian regolith using long-term diffusion and thermal cracking, *Icarus*, *179*, 387–397, doi:10.1016/j.icarus.2005.07.024.

Han, S.-C., N. Schmerr, G. Neumann, and S. Holmes (2014), Global characteristics of porosity and density stratification within the lunar crust from GRAIL gravity and Lunar Orbiter Laser Altimeter topography data, *Geophys. Res. Lett.*, *41*, 1882–1889, doi:10.1002/2014GL059378.

Head, J. W., J. F. Mustard, M. A. Kreslavsky, R. E. Milliken, and D. R. Marchant (2003), Recent ice ages on Mars, *Nature*, *426*, 797–802, doi:10.1038/nature02114.

Holt, J. W., M. E. Peters, S. D. Kempf, D. L. Morse, and D. D. Blankenship (2006), Echo source discrimination in single-pass airborne radar sounding data from the Dry Valleys, Antarctica: Implications for orbital sounding of Mars, *J. Geophys. Res.*, *111*, E06S24, doi:10.1029/2005JE002525.

Holt, J. W., et al. (2008), Radar sounding evidence for buried glaciers in the southern mid-latitudes of Mars, *Science*, *322*, 1235–1238.

Hudson, T. L., O. Aharonson, N. Schorghofer, C. B. Farmer, M. H. Hecht, and N. T. Bridges (2007), Water vapor diffusion in Mars subsurface environments, *J. Geophys. Res.*, *112*, E05016, doi:10.1029/2006JE002815.

Kadish, S. J., N. G. Barlow, and J. W. Head (2009), Latitude dependence of Martian pedestal craters: Evidence for a sublimation-driven formation mechanism, *J. Geophys. Res.*, *114*, E10001, doi:10.1029/2008JE003318.

Kirk, R. L., et al. (2008), Ultrahigh resolution topographic mapping of Mars with MRO HiRISE stereo images: Meter-scale slopes of candidate Phoenix landing sites, *J. Geophys. Res.*, *113*, E00A24, doi:10.1029/2007JE003000.

Levrard, B., F. Forget, F. Montmessin, and J. Laskar (2004), Recent ice-rich deposits formed at high latitudes on Mars by sublimation of unstable equatorial ice during low obliquity, *Nature*, *431*, 1072–1075, doi:10.1038/nature03055.

Madeleine, J.-B., F. Forget, J. W. Head, B. Levrard, F. Montmessin, and E. Millour (2009), Amazonian northern mid-latitude glaciation on Mars: A proposed climate scenario, *Icarus*, *203*, 390–405, doi:10.1016/j.icarus.2009.04.037.

Malin, M. C., et al. (2007), Context Camera Investigation on board the Mars Reconnaissance Orbiter, *J. Geophys. Res.*, *112*, E05S04, doi:10.1029/2006JE002808.

Matsuoka, T., S. Fujita, and S. Mae (1997), Dielectric properties of ice containing ionic impurities at microwave frequencies, *J. Phys. Chem. B*, *101*, 6219–6222, doi:10.1021/jp9631590.

McEwen, A. S., et al. (2010), The High Resolution Imaging Science Experiment (HiRISE) during MRO's Primary Science Phase (PSP), *Icarus*, *205*, 2–37, doi:10.1016/j.icarus.2009.04.023.

Mellon, M. T., and B. M. Jakosky (1993), Geographic variations in the thermal and diffusive stability of ground ice on Mars, *J. Geophys. Res.*, *98*(E2), 3345–3364, doi:10.1029/92JE02355.

Mellon, M. T., W. C. Feldman, and T. H. Prettyman (2004), The presence and stability of ground ice in the southern hemisphere of Mars, *Icarus*, *169*, 324–340, doi:10.1016/j.icarus.2003.10.022.

Mellon, M. T., et al. (2009), Ground ice at the Phoenix landing site: Stability state and origin, *J. Geophys. Res.*, *114*, E00E07, doi:10.1029/2009JE003417.

Mitrofanov, I., et al. (2002), Maps of subsurface hydrogen from the high energy neutron detector, Mars Odyssey, *Science*, *297*, 78–81, doi:10.1126/science.1073616.

Moore, H. J., and B. M. Jakosky (1989), Viking landing sites, remote-sensing observations, and physical properties of Martian surface materials, *Icarus*, *81*, 164–184, doi:10.1016/0019-1035(89)90132-2.

Moore, H. J., R. E. Hutton, G. D. Clow, and C. R. Spitzer (1987), Physical properties of the surface materials at the Viking landing sites on Mars, *U.S. Geol. Surv. Prof. Pap.*, *1389*, 1–222.

Ormö, J., A. P. Rossi, and K. R. Housen (2013), A new method to determine the direction of impact: Asymmetry of concentric impact craters as observed in the field (Lockne), on Mars, in experiments, and simulations, *Meteorit. Planet. Sci.*, *48*(3), 403–419, doi:10.1111/maps.12065.

Pettinelli, E., G. Vannaroni, A. Cereti, F. Paolucci, G. Della Monica, M. Storini, and F. Bella (2003), Frequency and time domain permittivity measurements on solid CO_2-soil mixtures as Martian soil simulants, *J. Geophys. Res.*, *108*(E4), 8029, doi:10.1029/2002JE001869.

Plaut, J. J., A. Safaeinili, B. A. Campbell, R. J. Phillips, N. E. Putzig, D. C. Nunes, and R. Seu (2009a), A widespread radar-transparent layer detected by SHARAD in Arcadia Planitia, Mars, paper presented at the 40th Lunar and Planetary Science Conference, Lunar and Planetary Institute, The Woodlands, Tex.

Plaut, J. J., A. Safaeinili, J. W. Holt, R. J. Phillips, J. W. Head, R. Seu, N. E. Putzig, and A. Frigeri (2009b), Radar evidence for ice in lobate debris aprons in the mid-northern latitudes of Mars, *Geophys. Res. Lett.*, *36*, L02203, doi:10.1029/2008GL036379.

Putzig, N. E., R. J. Phillips, B. A. Campbell, J. W. Holt, J. J. Plaut, L. M. Carter, A. F. Egan, F. Bernardini, A. Safaeinili, and R. Seu (2009), Subsurface structure of Planum Boreum from Mars Reconnaissance Orbiter Shallow Radar soundings, *Icarus*, *204*, 443–457, doi:10.1016/j.icarus.2009.07.034.

Quaide, W. L., and V. R. Oberbeck (1968), Thickness determinations of the lunar surface layer from lunar impact craters, *J. Geophys. Res.*, *73*(16), 5247–5270, doi:10.1029/JB073i016p05247.

Rust, A. C., J. K. Russell, and R. J. Knight (1999), Dielectric constant as a predictor of porosity in dry volcanic rocks, *J. Volcanol. Geotherm. Res.*, *91*, 79–96, doi:10.1016/S0377-0273(99)00055-4.

Schorghofer, N. (2007), Dynamics of ice ages on Mars, *Nature*, *449*, 192–194, doi:10.1038/nature06082.

Schorghofer, N., and F. Forget (2012), History and anatomy of subsurface ice on Mars, *Icarus*, *220*, 1112–1120, doi:10.1016/j.icarus.2012.07.003.

Schorghofer, N., and O. Aharonson (2005), Stability and exchange of subsurface ice on Mars, *J. Geophys. Res.*, *110*, E05003, doi:10.1029/2004JE002350.

Shabtaie, S., and C. R. Bentley (1994), Unified theory of electrical conduction in firn and ice: Site percolation and conduction in snow and firn, *J. Geophys. Res.*, *99*(B10), 19,757–19,769, doi:10.1029/94JB01510.

Sizemore, H. G., and M. T. Mellon (2008), Laboratory characterization of the structural properties controlling dynamical gas transport in Mars-analog soils, *Icarus*, *197*, 606–620, doi:10.1016/j.icarus.2008.05.013.

Sizemore, H. G., A. P. Zent, and A. W. Rempel (2015), Initiation and growth of Martian ice lenses, *Icarus*, *251*, 191–210, doi:10.1016/j.icarus.2014.04.013.

Smith, P. H., et al. (2009), H_2O at the Phoenix landing site, *Science*, *325*, 58–61, doi:10.1126/science.1172339.

Stillman, D. E., and R. E. Grimm (2011), Radar penetrates only the youngest geological units on Mars, *J. Geophys. Res.*, *116*, E03001, doi:10.1029/2010JE003661.

Stillman, D. E., R. E. Grimm, and S. F. Dec (2010), Low-frequency electrical properties of ice-silicate mixtures, *J. Phys. Chem. B*, *114*, 6065–6073, doi:10.1021/jp9070778.

Stillman, D., and G. Olhoeft (2008), Frequency and temperature dependence in electromagnetic properties of Martian analog minerals, *J. Geophys. Res.*, *113*, E09005, doi:10.1029/2007JE002977.

Sutton, S., R. Heyd, A. Fennema, A. S. Mcewen, R. L. Kirk, E. Howington-Kraus, A. Espinoza, and H. R. I. S. E. Team (2015), HiRISE digital terrain models: Updates and advances, paper presented at Second Planetary Data Workshop, Univ. Space Research Assoc, Flagstaff, Ariz.

Viola, D., A. S. McEwen, C. M. Dundas, and S. Byrne (2015), Expanded secondary craters in the Arcadia Planitia region Mars: Evidence for tens of Myr-old shallow subsurface ice, *Icarus*, *248*, 190–204, doi:10.1016/j.icarus.2014.10.032.

Watters, T. R., et al. (2007), Radar sounding of the Medusae Fossae Formation Mars: Equatorial ice or dry, low-density deposits?, *Science*, *318*, 1125–1128, doi:10.1126/science.1148112.

Wieczorek, M. A., et al. (2013), The crust of the Moon as seen by GRAIL, *Science*, *339*, 671–675, doi:10.1126/science.1231530.

Zent, A. P., M. H. Hecht, D. R. Cobos, S. E. Wood, T. L. Hudson, S. M. Milkovich, L. P. DeFlores, and M. T. Mellon (2010), Initial results from the thermal and electrical conductivity probe (TECP) on Phoenix, *J. Geophys. Res.*, *115*, E00E14, doi:10.1029/2009JE003420.